

Permanent-Magnet Coupled Power Inductor for Multiphase DC–DC Power Converters

Zhigang Dang, *Student Member, IEEE*, and Jaber A. Abu Qahouq, *Senior Member, IEEE*

Abstract—Using a coupled power inductor (CPI) in a multiphase dc–dc power converter instead of using multiple single-phase power inductors (PIs) reduces the inductor size and achieves better steady state and transient performances. To further reduce the inductor size and weight used in multiphase power converters, this paper presents a two-phase CPI that utilizes a permanent magnet (PM) to achieve almost doubled saturation current with the same size or equivalently achieve significant size and weight reduction. Operation principle of the presented permanent magnet coupled power inductor (PMCI) and required PM dimensions are derived and used as a design guide. The three-dimensional physical model of the PMCI is developed by using ANSYS/Maxwell software package to “visualize” the saturation current doubling. The fabricated PMCI design, with specifications of 24 A/phase, $\sim 4.25 \mu\text{H}/\text{phase}$ equivalent steady-state inductance, and $\sim 2.3 \mu\text{H}$ equivalent transient inductance, is tested in a 4–8 V two-phase dc–dc boost power converter with up to 50 A input current. Results show that compared to a conventional CPI design with the same size, weight, and inductance, the fabricated PMCI almost doubles the saturation current (from 13 to 24 A/phase). Compared to another CPI with a larger size but with even a smaller saturation current (18 A/phase), the core volume of the PMCI is reduced to 51.9% and the core weight is reduced to 51.2%. In addition, the PMCI achieves $\sim 76.3\%$ core size and $\sim 73.4\%$ core weight reductions compared to two separate single-phase PIs with the same steady-state inductance and similar saturation current (~ 22 A) due to the dual flux cancelation effect from the coupling and PM realized by the presented PMCI structure.

Index Terms—Boost converter, coupled power inductor (CPI), dc–dc converter, finite-element analysis (FEA), inductor, magnetics, multiphase, permanent magnet (PM), permanent-magnet coupled power inductor (PMCI), permanent-magnet power inductor (PMPI), power converter, saturation current, thermal characteristics.

I. INTRODUCTION

POWER devices such as power inductors (PIs) and power field effect transistors performances are critical in switching power converter applications [1]–[29]. The PI is one of the

Manuscript received May 29, 2016; revised September 16, 2016; accepted October 3, 2016. Date of publication November 8, 2016; date of current version February 9, 2017.

The authors are with the Department of Electrical and Computer Engineering, College of Engineering, The University of Alabama, Tuscaloosa, AL 35487 USA (e-mail: dangzhigang1990@gmail.com; jaberq@eng.ua.edu).

Color versions of one or more of the figures in this paper are available online at <http://ieeexplore.ieee.org>.

Digital Object Identifier 10.1109/TIE.2016.2626364

largest and heaviest components in a switching power converter, and it accounts for much of the weight and the size of switching power converters. Several figures of merit are considered for the design of PIs including the inductance density, the current/power density, the dc resistance, the thermal characteristics, and the saturation current. In order to obtain higher inductance density, or in other words achieve the required inductance in as small area as possible, technologies such as integrated inductors, microfabricated inductor, on-chip inductor, and coupled inductor have emerged over the years [4]–[29]. Saturation current is related to the core structure as well as the magnetic core material, among other factors. For a given core structure and design, employing magnetic material with higher saturation flux density helps to obtain a higher saturation current [4]–[10]:

$$\begin{cases} v_1 = L_1 \frac{di_1}{dt} + M \frac{di_2}{dt} \\ v_2 = M \frac{di_1}{dt} + L_2 \frac{di_2}{dt} \end{cases} \quad (1-1)$$

$$\alpha = \frac{M}{L_s}. \quad (1-2)$$

In order to increase the saturation current for the single-phase PI further, one or more permanent magnets (PMs) have been used to partially cancel the winding fluxes [11]–[13]. This concept of the permanent magnet power inductor (PMPI) not only doubles the saturation current for a single-phase PI, but also reduces its volume and weight significantly [13]. However, the structure realization and performance of the coupled power inductor (CPI) with the PM have not been investigated in the literature before, which is the main objective of this paper.

In a two-phase CPI, the two coupling types are illustrated in Fig. 1(a) and (b), where $L_1 = L_2 = L_s$ is self-inductance and M is mutual inductance. Both types can be described by (1-1), where v_1 and v_2 are the voltages applied to the two corresponding windings of the CPI as shown in Fig. 1(a) and (b). Coupling factor α is determined by (1-2). Both M and α are positive for the direct coupling and negative for the inverse coupling. Inversely coupled CPI is used in multiphase power converters [20]–[28]. Fig. 1(c) illustrates the utilization of the CPI in a two-phase boost power converter. Instead of using two separate PIs for two phases, only one CPI with two coupled windings is needed, which helps to reduce the total volume occupied by PIs and therefore results in a power converter with higher power density. The volume reduction of the CPI is because 1) two separate inductors are integrated into one core structure which

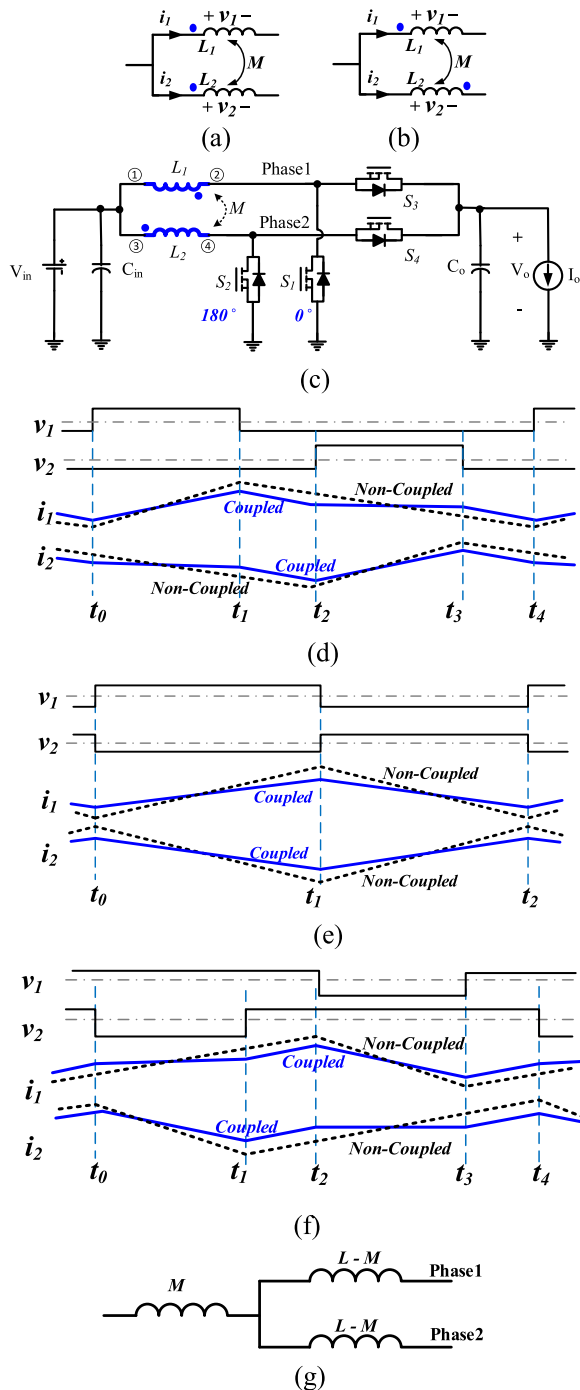


Fig. 1. Coupled inductor with (a) direct coupling and (b) inverse coupling. (c) Schematic of a boost converter using inversely coupled CPI and its steady-state operation waveforms with (d) $D < 0.5$, (e) $D = 0.5$ and (f) $D > 0.5$. (g) Equivalent circuit of transient inductance.

reduces footprint, and 2) the inverse coupling results in flux cancellation, which increases the saturation current of the CPI and equivalently reduces volume.

In order to review the advantage of using the CPI in a multiphase dc–dc power converter, the operation of the example boost converter using CPI is briefly summarized next in this section. Note that detailed operations for both multiphase buck converter and boost converter using coupled inductor have been extensively presented in the literature [20]–[28]. Fig. 1(d) and

(f) shows the steady-state operation waveforms of the dc–dc power converter with a CPI when the duty cycle $D < 0.5$, $= 0.5$, and > 0.5 . Control signal of S_1 and S_2 are 180° out of phase. S_1 and S_3 are turned ON and OFF complementary, and S_2 and S_4 are turned ON and OFF complementary as well. Consider the case when $D < 0.5$ as an example, during the time interval $t_0 \sim t_1$, S_1 is turned ON and S_2 is turned OFF, and the inductor current i_1 of phase 1 rises (inductor is charged) and inductor current i_2 of phase 2 decreases (inductor is discharged), but slopes of i_1 and i_2 are smaller while using the CPI compared to the noncoupled case because of the effect of the inverse coupling. During the time interval $t_1 \sim t_2$, both S_1 and S_2 are turned OFF, and the slopes of the two inductor currents in the two phases are the same when using the CPI and when using two separate PIs that are not coupled. During the time interval $t_2 \sim t_3$, S_1 is turned OFF and S_2 is turned ON, i_1 decreases and i_2 rises, but slopes of i_1 and i_2 are smaller when using the CPI compared to the noncoupled case because of the inverse coupling. During the time interval $t_3 \sim t_4$, both S_1 and S_2 are turned OFF again and the slope of inductor currents are the same again. In a complete switching cycle, the peak-to-peak value of the inductor current ripple is smaller when using a CPI than when using two separate PIs because of inverse coupling. This is the case when $D < 0.5$, $= 0.5$, and > 0.5 , i.e., the current ripple can be smaller under different duty cycle values. The amount of decrease in the steady-state inductor current ripple is dependent on both the duty cycle value and the coupling factor value [20]–[28]. The equivalent steady-state inductance (L_{SS}) of a CPI is the inductance measured between the two terminals [① and ② for L_1 , ③ and ④ for L_2] as illustrated in Fig. 1(c) for each phase of the CPI, which can also be determined by (2-1), where T_{on} is the on time of the control MOSFET, i.e., S_1 and S_2 in Fig. 1(c), and Δi is the peak-to-peak ripple of the inductor current for each phase. The smaller steady-state inductor current ripple values of the two-phase boost converter while using the CPI, as illustrated in Fig. 1(d) and (f), show that using the CPI results in larger equivalent steady-state inductance than using uncoupled inductors. This is advantageous for smaller steady-state inductor current ripple and higher power efficiency. Note that the average inductor currents, or dc component, of i_1 and i_2 are tuned by a closed-loop controller to be equal, as illustrated in Fig. 1(d) and (f) in order to equally distribute the thermal stress between two phases

$$L_{SS} = \frac{V_{in} T_{on}}{\Delta i} \quad (2-1)$$

$$L_{tr} = (1 + \alpha)L_S. \quad (2-2)$$

During transient operation, duty cycle is perturbed by the amount ΔD by the closed-loop controller that regulates the output voltage and maintains equal current distribution between the phases. The resulting amount of change in the average inductor current is determined by an equivalent inductance, which is referred to as equivalent transient inductance (L_{tr}). Fig. 1(g) illustrates the equivalent circuit of the transient inductance of a CPI, from which the per-phase L_{tr} is derived in (2-2) [22]. The amount of the change in inductor current when using a

CPI is larger than it is when using two separate PIs. This is because the CPI has a transient inductance value that is smaller than the steady-state inductance value (for a PI with no coupling, the steady-state inductance and the transient inductance are equal). This implies that using a CPI allows for achieving faster dynamic/transient response compared to when using two noncoupled PIs, which is an advantage.

This paper presents and investigates a structure for the permanent magnet coupled power inductor (PMCI), which utilizes a PM to either double the saturation current or equivalently reduces the size and weight of the CPI (or a mix of both). A PMCI with NdFeB-N35EH PM is developed, fabricated, and experimentally evaluated in a 4 V/8 V dc-dc boost power converter. Operation principle and magnetic circuit model of the PMCI and the dimensions of the required PM are theoretically devised and used as design guidelines. Three dimensional (3-D) physical model simulation results are used to “visualize” the saturation current doubling of the PMCI. Experimental results validate the proposed method. This paper considers all of design metrics for PIs including tradeoffs between size, efficiency, inductance density, and saturation current when evaluating the PMCI and comparing it to other PIs.

The method of inductor core biasing using an extra winding with controllable current, as presented in [29], can control the inductance values of the inductor under different operation states and achieve saturation current increase. However, the needed extra winding, power source/circuit, and fast controller to adjust the biasing leads to added size, weight, and power losses. On the other hand, the PMCI is able to double the saturation current or equivalently reduce the inductor size significantly without size increase and with negligible weight increase and power loss increase because of the PM. While the extra winding based inductor core biasing requires a high-speed controller which controls the injected dc flux for the inductor instantaneously when load varies or during fast load transient (which increases its design complexity), the PMCI does not require control. The PMCI maintains all the advantages of using an inversely CPI in a two-phase dc-dc power converter including high steady-state inductance to transient inductance ratio for higher power efficiency and reduced transient inductance to improve the transient performance while achieving smaller size and weight or higher saturation current.

II. CONCEPTS AND THEORETICAL ANALYSIS

A. Structure and Operation Principle of the PMCI

Fig. 2(a) illustrates the front-view diagram of the conventional CPI with the EE core structure. There are three gaps in each inductor, i.e., central gap g_c , left-side gap g_1 , and right-side gap g_2 . Using airgaps in a CPI core helps to 1) increase the saturation current as it is the case in single-phase PIs, and 2) tune the coupling factor between the two phases because coupling factor is dependent on the dimensions of airgaps in the central leg and the side legs. A larger central leg airgap and smaller side leg airgaps lead to a larger coupling factor magnitude, and vice versa. The per-phase input currents I_{dc1} and I_{dc2} and their directions are marked in Fig. 2(a) (shown on each of the side legs

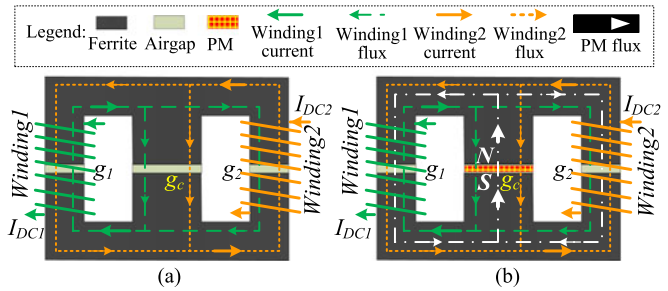


Fig. 2. Schematic diagram of core structure and dc flux lines in (a) CPI and (b) PMCI core (front view).

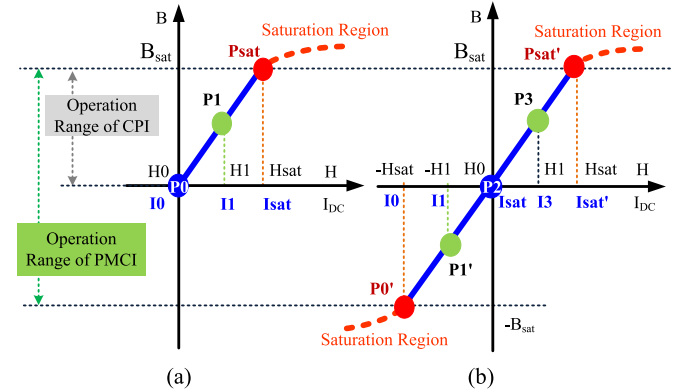


Fig. 3. Operation range of (a) CPI and (b) PMCI core on BH curve.

of the core). The fluxes generated by winding1 and winding2 are represented by the dashed arrowed green line and dotted arrowed orange line, respectively. Fig. 2(a) shows that the fluxes of winding1 and winding2 partially cancel with each other in two side legs, resulting in inverse coupling between two phases of a CPI and contribute to the size reduction of the CPI. Fig. 2(a) also shows that part of fluxes of winding1 and winding2 superimpose in the central core leg, leading to the saturation of the CPI core when per-phase winding current reaches to a certain level, which is referred to as saturation current. If a dc magnetic flux source is added in the central leg of the CPI such that winding fluxes can be partially/fully canceled, then the saturation current of the CPI can be increased. A piece of PM is able to provide the required dc magnetic flux source.

By placing a small piece of a PM in the central gap of the CPI, a PMCI is obtained as illustrated in Fig. 2(b). The PM needs to have properties as will be described in Section II-C. The dash-dotted arrowed white line denotes the flux path generated by the PM. The PM needs to be placed in the correct polarities such that its flux loops and winding flux loops are in opposite directions. As a result, the winding fluxes and the PM flux partially or completely cancel out, resulting in a significant increase in the saturation current compared to the CPI. When the PMCI is well designed, its saturation current can potentially be doubled compared to a conventional CPI. Due to the PM flux cancellation effect in addition to the windings' flux cancellations, the PMCI can achieve more size reduction compared with the CPI.

Fig. 3 illustrates the operation range of the CPI and PMCI cores on their BH curves, where hysteresis characteristics for the magnetic core material are neglected in this principle analysis.

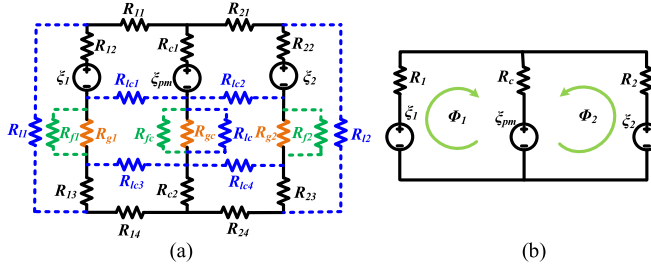


Fig. 4. Magnetic circuit models of the proposed PMCI: (a) complex model and (b) simplified model.

Same core material is used in the CPI and the PMCI for fair comparison. It is known that the magnetic flux density $B = \mu \cdot H$, where μ is magnetic permeability of the material and H is the applied magnetic field. H is directly proportional to the per-phase winding current. B_{sat} is the saturation flux density of the magnetic core material, H_{sat} is the corresponding magnetic field, and I_{sat} is the corresponding saturation current. In Fig. 3, a series of points including P_0 , P_1 , P_{sat} , P_0' , P_1' , P_2 , P_3 , and $P_{sat'}$ denote the operation points of the CPI and the PMCI for different I_{dc} values including I_0 , I_1 , I_{sat} , I_3 , and $I_{sat'}$. When $I_{dc} = I_0 = 0$, the CPI core operates at P_0 with zero flux density while the PMCI core operates at P_0' with flux density value of $-B_{sat}$ because the PM flux exists. This means that the PMCI core is prebiased by using the PM to its $-B_{sat}$ point when the input current is zero. When $I_{dc} = I_{sat}$, the CPI core operates at P_{sat} and starts to saturate while the PMCI core operates at P_2 with zero net flux density. The zero net flux density results from the flux cancellation between the winding fluxes and the PM flux because they are in opposite directions as illustrated in Fig. 2(b). When $I_{dc} = I_{sat'} = 2 \times I_{sat}$, the CPI core is deeply/highly saturated while the PMCI core is just starting to saturate. It can be observed from Fig. 3 that the operation range of the CPI core is limited in the first quadrant on the BH curve, while the PMCI core extends its operation range into the third quadrant because of the PM flux cancellation effect. As a result, the PMCI core has twice the operation range compared with the CPI core. This results in the effect of saturation current doubling, i.e., $I_{sat_PMCI} = 2 \times I_{sat_CPI}$, which is further analyzed in the next part of this section based on the magnetic circuit model and is verified by using ANSYS/Maxwell 3-D physical model simulation results as shown in Section III and the experimental results presented in Section IV.

B. Magnetic Circuit Model Analysis

The magnetic circuit model for the presented PMCI illustrated in Fig. 2(b) is shown in Fig. 4. In the complex model shown in Fig. 4(a), R_{11} , R_{12} , R_{13} , R_{14} , R_{21} , R_{22} , R_{23} , R_{24} , R_{lc1} , and R_{lc2} are reluctances of magnetic core legs. R_{l1} , R_{l2} , R_{lc} , R_{lc1} , R_{lc2} , R_{lc3} , and R_{lc4} are leakage reluctances. R_{g1} , R_{g2} , and R_{gc} are reluctances of air gaps. R_{f1} , R_{f2} , and R_{fc} are fringe reluctances of three gaps. Calculations of fringe reluctances and leakage reluctances of the PIs are discussed in [25]. Fig. 4(a) can be simplified as shown in Fig. 4(b). $\xi_1 = N_1 I_1$ and $\xi_2 = N_2 I_2$

are magnomotive force (MMF) of winding1 and winding2, respectively. Φ is the magnetic flux and N is the number of winding turns. ξ_{pm} is the MMF of the PM. R_{lc1} , R_{lc2} , R_{lc3} , and R_{lc4} are much larger than the other reluctance values and can be treated as if each of them is equal to infinity. The rest of the reluctances are grouped into R_1 , R_2 , and R_c as

$$\begin{cases} R_1 = R_{11} + (R_{12} + R_{13} + (R_{g1} || R_{f1})) || R_{l1} + R_{14} \\ R_2 = R_{21} + (R_{22} + R_{23} + (R_{g2} || R_{f2})) || R_{l2} + R_{24} \\ R_c = R_{c1} + R_{c2} + (R_{gc} || R_{fc} || R_{lc}) \end{cases} \quad (3-1)$$

Reluctance values are determined by (3-2), where l_e and A_e are the effective length and effective cross section area of the magnetic flux path, respectively. $\mu_e = \mu_r \mu_o$ is the effective permeability, μ_r is relative permeability, and μ_o is the vacuum permeability

$$R = \frac{l_e}{\mu_e A_e} = \frac{l_e}{\mu_r \mu_o A_e}. \quad (3-2)$$

Inductance can be calculated from $L = \lambda/i = N^2/R$, where λ is flux linkage [30]. Self-inductance (L_s) for each phase is determined next. When winding1 exists alone, i.e., ξ_{pm} and ξ_2 are shorted, the equivalent reluctance R_{eq1} is calculated as

$$R_{eq1} = (R_1 + R_c || R_2) = \frac{R_1 (R_c + R_2) + R_c R_2}{R_c + R_2}. \quad (4-1)$$

When winding2 exists alone, i.e., ξ_{pm} and ξ_1 are shorted, the equivalent reluctance R_{eq2} is calculated as

$$R_{eq2} = (R_2 + R_c || R_1) = \frac{R_2 (R_c + R_1) + R_c R_1}{R_c + R_1}. \quad (4-2)$$

Symmetrical structure for the CPI is widely used in multi-phase power converters [20]–[28] and thus is further discussed in this paper. In a symmetrical structure, $N_1 = N_2 = N$ and $R_1 = R_2 = R$. Accordingly, R_{eq1} and R_{eq2} are simplified as given by

$$R_{eq} = R_{eq1} = R_{eq2} = \frac{R(2R_c + R)}{R_c + R}. \quad (5)$$

Self-inductances for phase 1 and phase 2 can then be determined from (6). When compared to the CPI, the side leg reluctances R_1 and R_2 of the PMCI remain unchanged. However, R_{gc} is affected by the PM. The permeability of the PM material (the relative permeability of NdFeB magnet is ~ 1.05) is only slightly higher than the permeability of the air. This means that the R_c values of the CPI and the PMCI are almost the same, but R_c is slightly higher for the PMCI because of the PM. As a result, the self-inductance values of the CPI and the PMCI are almost equal but the PMCI has slightly larger inductance as a result of placing the PM in the central leg gap of the PMCI core

$$L_S = L_{S1} = L_{S2} = \frac{N^2}{R_{eq}} = \frac{N^2(R_c + R)}{R(2R_c + R)}. \quad (6)$$

Mutual inductance can be calculated as [30]

$$M = M_{12} = \frac{N_1 \Phi_{12}}{I_2} = \frac{N_2 \Phi_{21}}{I_1} = M_{21} \quad (7)$$

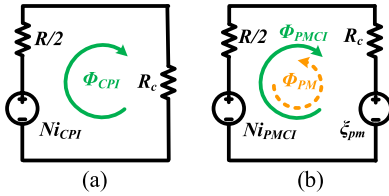


Fig. 5. Transformed magnetic circuit model of (a) CPI and (b) PMCI.

where Φ_{12} is the magnetic flux generated by I_2 that passes through winding1, and Φ_{21} is the magnetic flux generated by I_1 that passes through winding2. From Fig. 4(b), Φ_{12} and Φ_{21} are derived as

$$\Phi_{12} = \Phi_{21} = \frac{NI}{R_{\text{eq}}} \frac{R_c}{R + R_c} = NI \frac{R_c}{R(2R_c + R)}. \quad (8)$$

Based on (7) and (8), mutual inductance is derived as in (9). The negative sign in (9) comes from the inverse coupling between phase 1 and phase 2

$$M = M_{12} = M_{21} = -\frac{N^2 R_c}{R(2R_c + R)}. \quad (9)$$

The coupling factor (α) of the PMCI is derived as

$$\alpha = \frac{M}{L_s} = -\frac{R_c}{R_c + R}. \quad (10)$$

It can be observed from (9) and (10) that the mutual inductance and coupling factor values of the CPI and the PMCI are also the same. In order to derive the saturation current of the CPI and the PMCI, Fig. 4(b) is transformed into Fig. 5. By using Kirchhoff's voltage law, the following equations can be derived from circuit models as shown in Fig. 5:

$$Ni_{\text{CPI}} = \Phi_{\text{CPI}} \left(R_c + \frac{R}{2} \right) \quad (11-1)$$

$$Ni_{\text{PMCI}} - \xi_{\text{pm}} = (\Phi_{\text{PMCI}} - \Phi_{\text{PM}}) \left(R_c + \frac{R}{2} \right). \quad (11-2)$$

For the CPI and PMCI cores with effective cross section area of A_e , the total flux in the ferrite core is $\Phi = B \cdot A_e$, where B is the flux density in the magnetic core. Per-phase saturation current of the CPI and the PMCI is derived as

$$I_{\text{sat_CPI}} = \frac{B_{\text{sat}} A_e \left(R_c + \frac{R}{2} \right)}{N} \quad (12-1)$$

$$I_{\text{sat_PMCI}} = \frac{B_{\text{sat}} A_e \left(R_c + \frac{R}{2} \right) + \xi_{\text{pm}}}{N} \quad (12-2)$$

where B_{sat} is the saturation flux density of the PI core material.

In the PMCI design, ξ_{pm} has to satisfy $0 < \xi_{\text{pm}} \leq N \cdot I_{\text{sat_CPI}}$ to ensure the magnetic core is not saturated by the PM itself when winding current is zero. When $\xi_{\text{pm}} = N \cdot I_{\text{sat_CPI}}$, (12-2) can be rewritten as (13), which shows that the per-phase saturation current of the PMCI can be twice as large as the saturation current of the CPI with same windings and same magnetic core (indicating the same inductance, same size, and

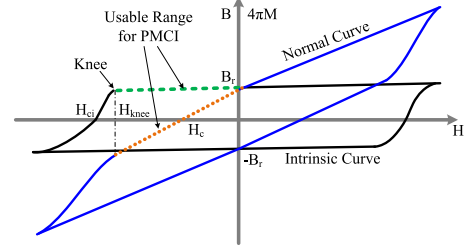


Fig. 6. Magnetic hysteresis loop of the PM.

same weight)

$$I_{\text{sat_PMCI}} = \frac{B_{\text{sat}} A_e \left(R_c + \frac{R}{2} \right)}{N} + I_{\text{sat_CPI}} = 2 \cdot I_{\text{sat_CPI}}. \quad (13)$$

C. Permanent Magnet Design for the PMCI

In the PMCI design, PM design is a critical step in order to achieve the saturation current doubling without reducing the inductance value. The PM used in the PMCI should have a BH characteristic with a wide hysteresis loop as shown in Fig. 6. The intrinsic curve represents the intrinsic magnetization $4\pi M$ (in Gaussian units) as a function of applied magnetic field (H). The normal curve represents B as a function of H . $B = \mu \cdot H = \mu_0 \cdot \mu_r \cdot H$ and $B = H + 4\pi M$ (in Gaussian units) [31]. B_r is the residual flux density, H_c is coercivity (the reverse field which will reduce B to zero), and H_{ci} is intrinsic coercivity (the reverse field required to reduce $4\pi M$ to zero). For PM materials, demagnetization occurs when a sufficient reverse H field is applied across the PM. When the operation point of the PM is driven to the left part (nonlinear part) of the “knee” point on the BH curve as shown in Fig. 6, the PM material will start to be irreversibly demagnetized. To avoid such demagnetization under any operation condition of the PMCI, PM materials with sufficiently high H_{ci} and H_{knee} values are needed. Usable/safe operation range of the PM for the PMCI design is marked on both the normal curve and intrinsic curve.

Similar with PM dimension design for the single-phase PMPI as detailed in [13], dimensions of the PM to be used for PMCI design can be determined based on the equivalent energy stored in the magnetic core and energy “supplied” by the PM. Maximum magnetic energy produced by a PM in the external space (E_{PM}) is determined by [31]

$$E_{\text{PM}} = \frac{(BH)_{\text{max}}}{2} V_{\text{PM}} \quad (14)$$

where $(BH)_{\text{max}}$ and V_{PM} represent maximum energy product and volume of the PM, respectively. The maximum magnetic energy stored in the CPI/PMCI core (E_{core}) is determined by [30]

$$E_{\text{core}} = \frac{B_{\text{sat}}^2}{2\mu_e} V_e \quad (15)$$

where μ_e and V_e are the effective permeability and effective volume of gapped magnetic core for each phase, respectively. To ensure the ferrite core is not saturated by the PM

TABLE I
CHARACTERISTICS OF THE PM

Parameter	Value	Parameter	Value
PM type	NdFeB-N35EH	H_{kne}	1989 kA/m
$(BH)_{max}$	188 kJ/m ³	B_r	1.06 T
H_c	574.8 kA/m	Mass density	7.5 g/cm ³
H_{ci}	2244.8 kA/m	Resistivity ρ_{PM}	180 $\mu\Omega \cdot cm$

itself, the relationship $E_{PM} \leq E_{core}$ has to be satisfied. Let $E_{core} = E_{PM}$, then the volume of the PM is derived as in (16) and the dimensions of the PM can be determined accordingly. When $E_{PM} = E_{core}$, maximum amount of flux cancellation can be achieved and saturation current can theoretically be doubled without saturating the inductor core by the PM itself. When $E_{PM} < E_{core}$, flux cancellation effect still exists but the potential of the PM in increasing the saturation current of the PI is not maximized. In other words, if $E_{PM} < E_{core}$, the saturation current increase would be less than double

$$V_{\text{PM}} = \frac{{B_{\text{sat}}}^2 V_e}{\mu_{\text{eff}} \cdot (BH)_{\text{max}}} \quad (16)$$

where a higher $(BH)_{\max}$ results in lower volume of the PM, which contributes to smaller weight and lower cost. Based on requirements for high H_{ci} , H_{knee} , and large $(BH)_{\max}$ values, NdFeB magnet is used in this work. The main characteristics of fabricated NdFeB-N35EH magnet at 300 K (\approx 26.8 °C) are listed in **Table I**.

D. Design Procedures of PMCI

Fig. 7(a) illustrates the design procedures for the PMCI. Substeps for CPI design and PMCI design are illustrated in **Fig. 7(b)** and **(c)**, respectively. Note that both CPI design process and PMCI design process are multistep iterative design processes, as it is the case for single-phase PI design [30].

III. 3-D PHYSICAL MODEL SIMULATION OF THE PMCI

The 3-D physical model developed in ANSYS/Maxwell for the PMCI design is shown in Fig. 8 and core dimensions are listed in Table II. The CPI and the PMCI use the same EE shaped ferrite core E 16/8/5 (EF 16) [32] from TDK and the ferrite material is N87 (B_{sat} is ~ 0.45 T at 25°C , resistivity is $10 \Omega\text{m}$, and density is $\sim 4850 \text{ kg/m}^3$) [33]. Both winding1 and winding2 have 8.5 turns of copper wire. The core shape, size, and windings are predetermined based on an example boost converter application which will be presented in the next section. Based on the datasheet specifications, effective quantities of the PMCI core are calculated as $\mu_{\text{eff}} = \sim 72.1 \cdot \mu_0$, $A_{\text{eff}} = 10 \text{ mm}^2$, and $l_{\text{eff}} = 40.7 \text{ mm}$. The required V_{PM} of NdFeB-N35EH magnet are calculated from (16) as $V_{\text{PM}} = 4.83 \text{ mm}^3$. The thickness of the fabricated NdFeB-N35EH magnet is 0.3 mm, then the length and width of the PM can be calculated as $\sim 4 \text{ mm}$.

Finite element analysis (FEA) results shown in Fig. 9(a) “visualize” the B field distribution of the CPI and PMCI cores when the dc input current increases from 0 to 30 A/phase. For the CPI,

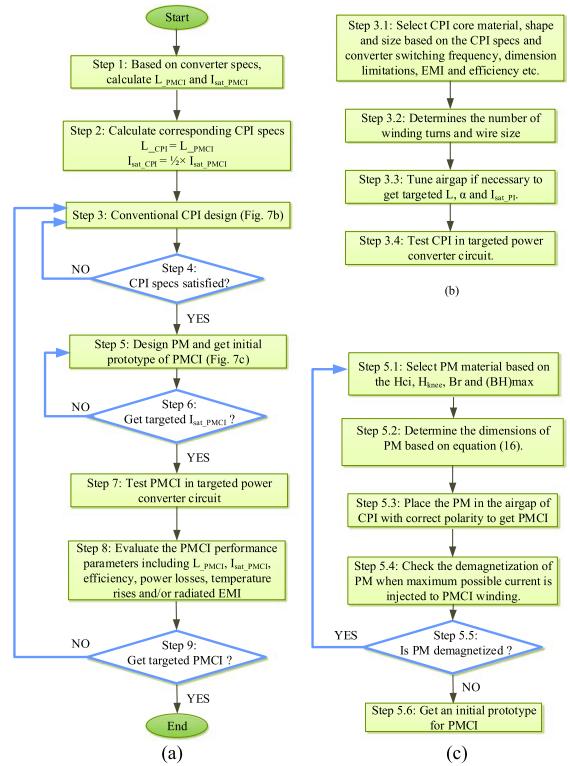


Fig. 7. Design procedures of the PMCI.

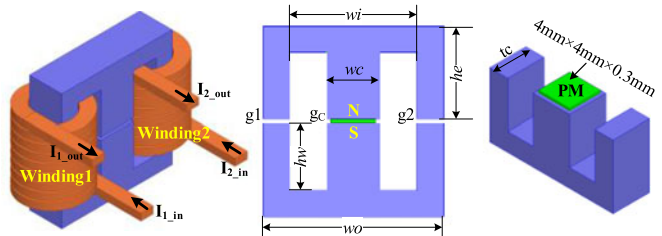
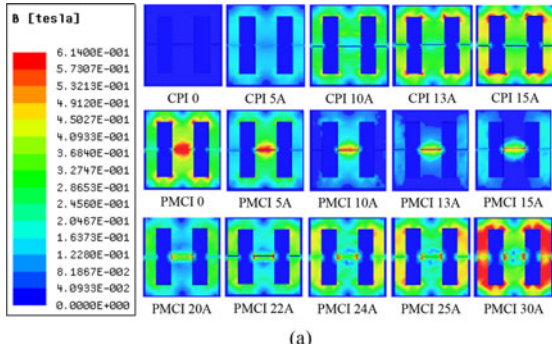


Fig. 8. 3-D physical model and design parameters of the PMCI.

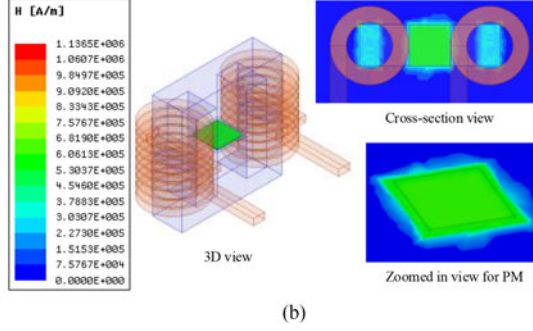
TABLE II
DIMENSIONS OF PMCI CORE

Parameter	Value	Parameter	Value
he	8.2 mm	hw	5.7 mm
wi	11.3 mm	wo	16 mm
wc	4.7 mm	tc	4.7 mm
$g1 = g2 = gc$	0.34 mm	PM	$4 \text{ mm} \times 4 \text{ mm} \times 0.3 \text{ mm}$

the magnitude of B increases with the increase of the dc input current and B values start to approach $B_{\text{sat}} = 0.45$ T when the dc input current is 13 A/phase. Namely, the saturation current of the CPI $I_{\text{satCPI}} = 13$ A/phase. For the PMCI, when the input current is 0, the ferrite core has significant amount of magnetic fluxes generated by the PM but is not saturated by the PM itself. When the input current increases from 0 to 30 A/phase, the net B value of the PMCI first decreases to a very small value at 13 A/phase then gradually increases. The PMCI core starts



(a)



(b)

Fig. 9. FEA simulation results: (a) B field of the CPI and the PMCI under various dc current/phases (fixed scaling) and (b) H field of the PM when dc current of the PMCI is 30 A/phase (auto-scaling).

to saturate when the input current is ~ 24 A/phase. The reason why the net flux reaches to its minimum at 13 A/phase is the cancellation effect between the winding fluxes and PM flux as illustrated in Section II-A. Simulation results show that saturation current of the PMCI (~ 24 A/phase) is almost twice as large as the saturation current of the CPI (~ 13 A/phase) which is consistent with the derivation in (13).

Demagnetization of the PM is checked when 30 A/phase is applied to the PMCI and resulting H field distribution as illustrated in Fig. 9(b). As discussed in Section II-C, the PM operates in its safe range as long as the H field magnitude in the PM is less than the value of H_{knee} , which is 1989 kA/m for the NdFeB-N35EH used in PMCI design at 26.8 °C. Fig. 9(b) shows that the maximum H value of the PM is 1137 kA/m $< H_{knee} = 1989$ kA/m. The H_{knee} value is calculated based on the temperature coefficient of NdFeB-N35EH [34] as 1375 kA/m when the PM operates at 100 °C, which is also larger than 1137 kA/m. This indicates that the PM used in the PMCI design operates in the safe range even when the input current is as high as 30 A/phase and the temperature is up to 100 °C. The highest hypothetical temperature, at which the fabricated NdFeB-N35EH is able to work safely at 30 A/phase, is calculated as 138 °C.

IV. EXPERIMENTAL RESULTS

Fabricated inductors and their dimensions are shown in Fig. 10. The PMCI is fabricated by inserting the designed PM in the central gap of the CPI. The characteristics of the fabricated NdFeB-N35EH magnet for the PMCI are specified in Table I

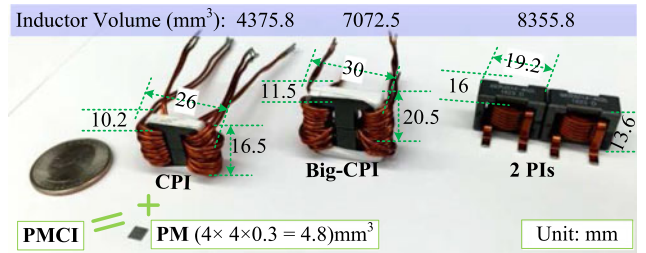


Fig. 10. Dimension specifications for power inductors.

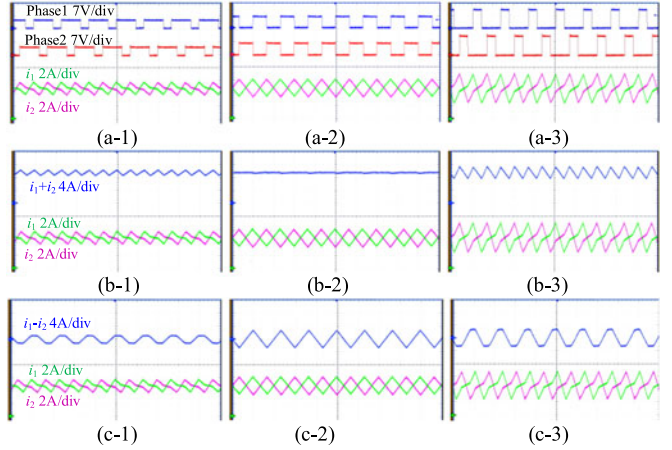


Fig. 11. Sample experimentally measured waveforms for phase node voltages and inductor currents (dc coupled) which are the same for both the CPI and the PMCI. $D = 0.3$ for (a-1), (b-1), (c-1). $D = 0.5$ for (a-2), (b-2), (c-2). $D = 0.7$ for (a-3), (b-3), (c-3).

and its dimensions are calculated in Section III-A. CPI that has bigger core but smaller saturation current compared with the PMCI, referred to as the Big-CPI, is used for size and weight comparison purpose. The side-leg gaps of the CPI, PMCI, and Big-CPI are filled with an insulation tape, which has almost the same permeability value as the air. The central leg gap of the CPI and the Big-CPI is filled with air, and the central leg gap of the PMCI is filled with NdFeB magnet and air. Note that the value of the relative permeability of NdFeB magnet (~ 1.05) is very close to that of the air (~ 1).

Two parallel solid magnetic copper wires with the size of AWG 18 are used for PI windings. Detailed core dimensions and core material used are specified in Section III. Two separate PIs (SER2014-402ML) from Coilcraft [35] are used for size and weight comparison purposes. A two-phase dc-dc boost power converter as illustrated in Fig. 1(c) is designed and fabricated in order to test and evaluate the PMCI. The fabricated converter's input voltage $V_{in} = 4$ V, switching frequency is 150 kHz, and input capacitor (C_{in}) and output capacitor (C_o) are 120 and 480 μ F, respectively. Fig. 11 shows sample waveforms for the two-phase boost converter when input current is 10 A. Since the measured waveforms when using the PMCI are experimentally verified to be the same as when using the CPI, only one group of waveforms are presented to avoid repetition of the same waveforms. Fig. 11(a) shows the waveforms measured for the

TABLE III
COMPARISONS OF FABRICATED POWER INDUCTORS

	CPI	PMCI	Big-CPI	2 Separate PIs
Core volume (mm^3)	1173.6	1173.6	2260	4950.4
Core volume reduction compared to two PIs (%)	–	76.3%	54.3%	–
Core weight (g)	3.78	3.816	7.45	14.37
Core weight reduction compared to two PIs (%)	–	73.4%	48.2%	–
Total inductor volume (mm^3)	4375.8	4375.8	7072.5	8355.8
Total inductor weight (g)	13.41	13.45	15.761	24.6
PM size (mm^3)	–	$4 \times 4 \times 0.3$ $= 4.8$	–	–
PM weight (g)	–	0.036	–	–
Self-Inductance L_s ($\mu\text{H}/\text{phase}$)	3.2	3.3	3.2	4
Coupling factor α	–0.29	–0.29	–0.29	0
DCR ($\text{m}\Omega/\text{phase}$) @ 25 °C	3.14	3.14	2.93	2
Equivalent steady-state inductance L_{SS} ($\mu\text{H}/\text{phase}$)	4.1	4.25	4.1	4.0
Equivalent transient inductance L_{tr} ($\mu\text{H}/\text{phase}$)	2.3	2.3	2.3	4
Saturation current (A/phase)*	13	24	18	22

Saturation current is defined as the inductor dc current with $\sim 10\%$ inductance drop.

phase node voltages and the inductor currents for phase 1 (i_1) and phase 2 (i_2) of the two-phase boost converter when $D = 0.3$, 0.5, and 0.7, respectively. Note that the shape and magnitude of inductor current ripples are affected by the duty cycle and they are the same for the CPI and the PMCI as expected. Fig. 11(b) shows the sum of two-phase inductors $i_1 + i_2$. Note that ripple values of $(i_1 + i_2)$ are affected by duty cycle. Fig. 11(c) shows the waveforms of $(i_1 - i_2)$. Note that the dc values of $(i_1 - i_2)$ are zero, because the currents of phase 1 and phase 2 are equal (balanced). The analysis and discussion in the rest of the paper are based on the application example when the input voltage $V_{in} = 4$ V and the output voltage $V_o = 8$ V, i.e., $D = 0.5$.

Some of the most important parameters and measured experimental results for the fabricated PIs are summarized in Table III for comparison. Results show that the sizes and inductance values of the PMCI and the CPI are the same, but the PMCI has almost double of the saturation current compared to the CPI (24 A/phase compared to 13 A/phase). The PMCI has slightly larger inductance and higher saturation current compared to the Big-CPI (18 A/phase), and achieves 48.1% core size reduction and 48.8% core weight reduction. The addition of the PM does not cause any size increase because it is placed in the airgap. The weight of the PM (36 mg) is 0.95% of the weight of the PMCI ferrite core, which means that the total weight increase of the PMCI due to the addition of the NdFeB-N35EH magnet is negligible. Compared to two separate PIs, the PMCI achieves 76.3% core size reduction and 73.4% core weight reduction. Detailed performance evaluations and comparisons are presented in the following sections.

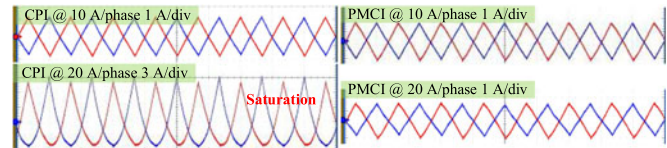


Fig. 12. Measured current waveforms for the CPI and the PMCI when power inductor current values are 10 and 20 A/phase (ac coupled).

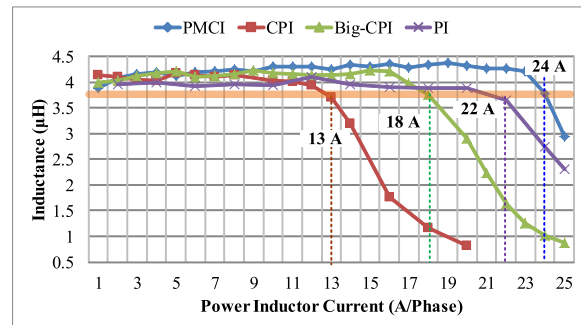


Fig. 13. Inductance values as a function of per-phase power inductor current.

A. Inductance and Saturation Current Measurements

The current value at which the inductor starts to saturate is identified when the inductance value drops by $\sim 10\%$. The per-phase equivalent steady-state inductance L_{SS} is determined based on (2-1). The measured PI current waveform samples are shown in Fig. 12. The waveform shapes are similar with the case that two separate inductors are used because duty cycle in this example application is 0.5, as illustrated in Fig. 1(d) and (f). It can be observed that when inductor is saturated, Δi is larger and the current waveform becomes nonlinear. The inductance values at different PI current values (from 1 to 25 A/phase) are calculated from the experimentally measured waveforms and are plotted in Fig. 13. The CPI has nearly constant inductance value of $\sim 4.1 \mu\text{H}/\text{phase}$ when current is less than its saturation current value 13 A/phase. The PMCI has nearly constant inductance value of $\sim 4.25 \mu\text{H}/\text{phase}$ when current is less than its saturation value 24 A/phase. This verifies magnetic circuit model analysis and 3-D physical model simulation results for saturation current doubling. The Big-CPI has nearly constant inductance value of $\sim 4.1 \mu\text{H}/\text{phase}$ before starting to saturate at 18 A/phase. The single-phase PI has nearly constant inductance value of $\sim 4.0 \mu\text{H}$ before starting saturation at 22 A.

During load transient, voltage overshoot or undershoot are suppressed by controller through varying the duty cycles dynamically. Because test results have shown that steady-state operation waveforms are the same in the case of the CPI and the PMCI with various duty cycles, transient waveforms will also be the same. In other words, equivalent transient inductance will be the same for the CPI and the PMCI as also supported by (2-2). Using (2-2), the calculated results are listed in Table III. Results show that the CPI, PMCI, and Big-CPI have the same L_{tr} value ($\sim 2.9 \mu\text{H}$), which is smaller than the L_{tr} value of the

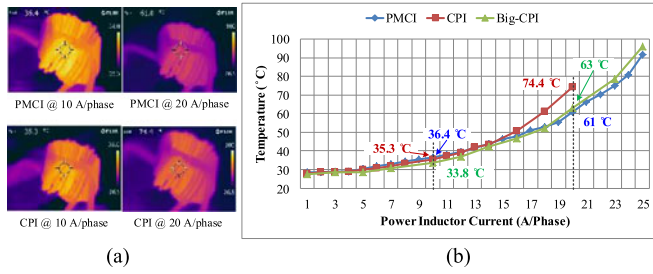


Fig. 14. (a) Temperature distribution images and (b) temperature as a function of per phase inductor current.

single-phase PI ($4 \mu\text{H}$). As a result, a power converter that uses a CPI, PMCI, or Big-CPI will have the same transient performance and will be better than when using two separate PIs.

B. Thermal Characteristics and Power Inductor Losses

Temperature rise values for the PIs at different current values are measured using a FLIR T-62101 thermal imaging camera. Sample temperature distribution images of the CPI and the PMCI are shown in Fig. 14(a). Based on the temperature measurement results, curves for the temperature rise as a function of per-phase inductor current are plotted, as shown in Fig. 14(b). It can be observed that the temperature increases with the increase of current for all PIs, as expected. When inductor current is less than the saturation current of the CPI (13 A/phase), all three inductors have similar temperature rise values but the temperature of the PMCI (T_{PMCI}) is slightly higher than temperatures of the CPI (T_{CPI}) and Big-CPI ($T_{\text{Big-CPI}}$). For example, at 10 A/phase, $T_{\text{PMCI}} = 36.4^\circ\text{C}$, $T_{\text{CPI}} = 35.3^\circ\text{C}$, and $T_{\text{Big-CPI}} = 33.8^\circ\text{C}$. This is because eddy current loss of the NdFeB-N35EH magnet contributes to the temperature rise of the PMCI due to its small resistivity ($\rho_{\text{PM}} = 180 \mu\Omega \cdot \text{cm}$). Meanwhile, there exists large dc bias in the B field of the PMCI core when inductor current is small because of the PM, as illustrated in Fig. 9(a). As a result, the core loss of the PMCI at small inductor current will be slightly increased, which also contributes to higher T_{PMCI} values. When inductor current is larger than 13 A/phase and smaller than the saturation current of the Big-CPI (18 A/phase), $T_{\text{Big-CPI}}$ has the smallest values because of its big size. T_{CPI} is larger than T_{PMCI} because the saturation of CPI core contributes to larger inductor current ripple and higher core and winding losses. When inductor current is larger than 18 A/phase, both T_{CPI} and $T_{\text{Big-CPI}}$ have larger values than T_{PMCI} . This is because both CPI and Big-CPI cores are saturated but PM cancels the magnetic flux in the PMCI core and helps to reduce the core and winding losses. For example, at 20 A/phase, $T_{\text{PMCI}} = 61^\circ\text{C}$, $T_{\text{CPI}} = 74.4^\circ\text{C}$, and $T_{\text{Big-CPI}} = 63^\circ\text{C}$.

Temperature rise values shown in Fig. 14(b) are good indication for total PI losses. It is also interesting to know the dc power losses (P_{dc}) of different PIs. DC winding resistance (DCR) of different PIs at 25°C is measured and is listed in Table III. The temperature (T)-dependent DCR per-phase can be determined from the equation $\text{DCR} = \text{DCR}_o \cdot (1 + \alpha(T - T_o))$ [13], where DCR_o is the DCR at temperature T_o , α is the temperature coefficient of the resistance, and for copper it is equal to $3.93 \times 10^{-3}/^\circ\text{C}$ [13]. P_{dc} values are calculated as follows and plotted in Fig. 15

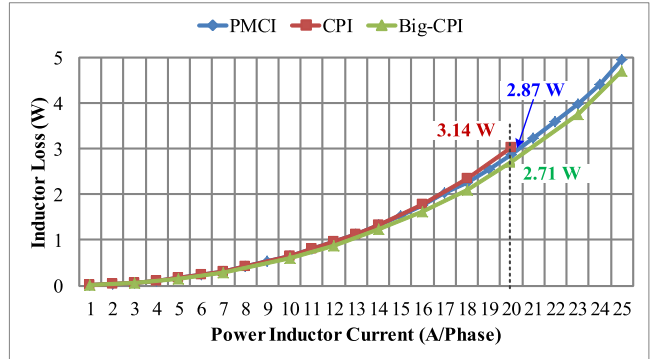


Fig. 15. Power inductor dc losses as a function of per-phase inductor current.

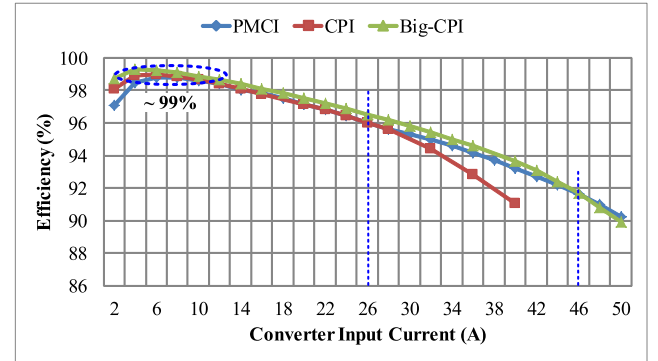


Fig. 16. Two-phase boost converter efficiencies (considering driver losses) as a function of load current.

$(T - T_o)$) [13], where DCR_o is the DCR at temperature T_o , α is the temperature coefficient of the resistance, and for copper it is equal to $3.93 \times 10^{-3}/^\circ\text{C}$ [13]. P_{dc} values are calculated as follows and plotted in Fig. 15

$$P_{\text{dc}} = (I_{\text{rms},1}^2 + I_{\text{rms},2}^2)(\text{DCR}_o(1 + \alpha(T - T_o))) \quad (17)$$

where $I_{\text{rms},1}$ and $I_{\text{rms},2}$ are measured root-mean-square (rms) values of PI current per-phase. Fig. 15 shows that P_{dc} values of all PIs increase with the increase of inductor current. The Big-CPI has the smallest P_{dc} because it has the shorter winding and smaller DCR than that of the CPI and the PMCI. The CPI and the PMCI have similar P_{dc} values before saturation of the CPI. When inductor current is larger than 13 A, namely after saturation of the CPI, the PMCI has smaller P_{dc} values, which is also supported by temperature rise values shown in Fig. 14.

C. Total Power Converter Efficiency

Two-phase boost power converter efficiencies are measured when using the PMCI and the CPI. Efficiencies are determined by using the following equation and measured efficiencies are plotted as a function of input current, as shown in Fig. 16:

$$\eta = \frac{P_o}{P_{\text{in}} + P_{\text{driver}}} = \frac{V_o \cdot I_o}{V_{\text{in}} \cdot I_{\text{in}} + V_{\text{driver}} \cdot I_{\text{driver}}} \quad (18)$$

where V_{in} is the input voltage measured at two terminals of input capacitor using a digital multimeter, I_{in} is the input current measured through the power supply, V_o is the output voltage measured across the two terminals of output capacitor using a digital multimeter (which is maintained at fixed value by slightly adjusting the duty cycle), and I_o is the output current measured from the dc electronic load used in the experiment. V_{driver} and I_{driver} are voltage and current of the gate drivers, respectively. Note that the converter input current is two times of the per-phase PI current. Results show that the power converter achieves $\sim 99\%$ peak efficiency with all three CPIs. The power converter with the CPI and the power converter with the PMCI have similar η values before saturation of the CPI. When converter input current is larger than 26 A, namely after saturation of the CPI, the converter with the PMCI starts to have higher efficiency. During light load conditions, i.e., when the converter input current is smaller than 6 A, the efficiency of the converter with the PMCI is less than 1% lower than the efficiency with the CPI due to the PM loss and larger PMCI losses because the PM contributes to larger dc bias of the B field, as explained in Section IV-B. The power converter with the Big-CPI has the highest efficiency when input current is less than 46 A. When input current further increases, the Big-CPI is largely saturated and power converter with the PMCI starts to have highest efficiency. Efficiency results also agree with temperature rise results shown in Fig. 14.

V. CONCLUSION

The presented PMCI was fabricated based on the guidelines derived from the developed magnetic circuit model and PM characteristics. Experimental results showed that the PMCI almost doubles the saturation current compared to the CPI (from 13 to 24 A/phase) with the same size, weight, and the same inductance. The PMCI also achieved 48.1% core size reduction and 48.8% core weight reduction compared to the Big-CPI with the same inductance but with a smaller saturation current (~ 18 A/phase). In addition, the PMCI achieved $\sim 76.3\%$ core size and $\sim 73.4\%$ core weight reductions compared to two separate single-phase PIs with the same steady-state inductance and similar saturation current, thanks to the dual flux cancelation effect from the coupling and PM realized by the presented PI structure.

It should be noted that the presented PMCI is suitable for unidirectional power converters with unidirectional power flow, and it is not suitable or intended for bidirectional power converters with bidirectional power flow. This is because in order for the design to double the saturation current, the flux density of the PMCI core is designed to be near the saturation flux density value when the current is zero. If the current flows in the opposite/negative direction, it will drive the PMCI core to saturation.

ACKNOWLEDGMENT

The authors would like to thank Y. Cao for his help in obtaining additional experimental results of Fig. 11.

REFERENCES

- [1] B. Zhao, Q. Song, and W. Liu, "Experimental comparison of isolated bidirectional dc–dc converters based on all-Si and all-SiC power devices for next-generation power conversion application," *IEEE Trans. Ind. Electron.*, vol. 61, no. 3, pp. 1389–1393, Mar. 2014.
- [2] Y. Nakakohara, H. Otake, T. M. Evans, T. Yoshida, M. Tsuruya, and K. Nakahara, "Three-phase LLC series resonant dc/dc converter using SiC MOSFETs to realize high-voltage and high-frequency operation," *IEEE Trans. Ind. Electron.*, vol. 63, no. 4, pp. 2103–2110, Apr. 2016.
- [3] O. Khan, W. Xiao, and H. H. Zeineldin, "Gallium–nitride-based submodule integrated converters for high-efficiency distributed maximum power point tracking PV applications," *IEEE Trans. Ind. Electron.*, vol. 63, no. 2, pp. 966–975, Feb. 2016.
- [4] S. C. O. Mathuna, T. O'Donnell, N. Wang, and K. Rinne, "Magnetics on silicon: An enabling technology for power supply on chip," *IEEE Trans. Power Electron.*, vol. 20, no. 3, pp. 585–592, May 2005.
- [5] C. O. Mathuna, N. N. Wang, S. Kulkarni, and S. Roy, "Review of integrated magnetics for power supply on chip (PwrSoC)," *IEEE Trans. Power Electron.*, vol. 27, no. 11, pp. 4799–4816, Nov. 2012.
- [6] L. Tan, N. Zhu, and B. Wu, "An integrated inductor for eliminating circulating current of parallel three-level dc–dc converter based EV fast charger," *IEEE Trans. Ind. Electron.*, vol. 63, no. 3, pp. 1362–1371, Mar. 2016.
- [7] G. Gohil, L. Bede, R. Teodorescu, T. Kerekes, and F. Blaabjerg, "An integrated inductor for parallel interleaved VSCs and PWM schemes for flux minimization," *IEEE Trans. Ind. Electron.*, vol. 62, no. 12, pp. 7534–7546, Dec. 2015.
- [8] P. Herget *et al.*, "A study of current density limits due to saturation in thin film magnetic inductors for on-chip power conversion," *IEEE Trans. Magn.*, vol. 48, no. 11, pp. 4119–4122, Nov. 2012.
- [9] A. Camarda, E. Macrelli, A. Romani, and M. Tartagni, "Design optimization of integrated magnetic core inductors," *IEEE Trans. Magn.*, vol. 51, no. 7, Jul. 2015, Art. no. 8401010.
- [10] G. Di Capua and N. Femia, "A novel method to predict the real operation of ferrite inductors with moderate saturation in switching power supply applications," *IEEE Trans. Power Electron.*, vol. 31, no. 3, pp. 2456–2464, Mar. 2016.
- [11] J. T. Ludwing, "Inductor biased with permanent magnets: Part I-Theory and analysis," *Trans. Amer. Inst. Elect. Eng., Commun. Electron.*, vol. 79, no. 3, pp. 273–278, Jul. 1960.
- [12] G. M. Shand and S. D. Sudhoff, "Design paradigm for permanent-magnet-inductor-based power converters," *IEEE Trans. Energy Convers.*, vol. 28, no. 4, pp. 880–893, Dec. 2013.
- [13] Z. Dang and J. Abu Qahouq, "Evaluation of high-current toroid power inductor with NdFeB magnet for dc–dc power converters," *IEEE Trans. Ind. Electron.*, vol. 62, no. 11, pp. 6868–6876, Nov. 2015.
- [14] J. Ewanchuk and J. Salmon, "Three-limb coupled inductor operation for paralleled multi-level three-phase voltage sourced inverters," *IEEE Trans. Ind. Electron.*, vol. 60, no. 5, pp. 1979–1988, May 2013.
- [15] M. Mohammadi and H. Farzanehfard, "New family of zero-voltage-transition PWM bidirectional converters with coupled inductors," *IEEE Trans. Ind. Electron.*, vol. 59, no. 2, pp. 912–919, Feb. 2012.
- [16] H. Wu, K. Sun, L. Chen, L. Zhu, and Y. Xing, "High step-up/step-down soft-switching bidirectional dc–dc converter with coupled-inductor and voltage matching control for energy storage systems," *IEEE Trans. Ind. Electron.*, vol. 63, no. 5, pp. 2892–2903, May 2016.
- [17] S. M. Chen, T. J. Liang, L. S. Yang, and J. F. Chen, "A boost converter with capacitor multiplier and coupled inductor for ac module applications," *IEEE Trans. Ind. Electron.*, vol. 60, no. 4, pp. 1503–1511, Apr. 2013.
- [18] G. Chen, Y. Deng, Y. Tao, X. He, Y. Wang, and Y. Hu, "Topology derivation and generalized analysis of zero-voltage-switching synchronous dc–dc converters with coupled inductors," *IEEE Trans. Ind. Electron.*, vol. 63, no. 8, pp. 4805–4815, Aug. 2016.
- [19] G. Di Capua and N. Femia, "A critical investigation of coupled inductors SEPIC design issues," *IEEE Trans. Ind. Electron.*, vol. 61, no. 6, pp. 2724–2734, Jun. 2014.
- [20] G. Spiazzi and S. Buso, "Analysis of the interleaved isolated boost converter with coupled inductors," *IEEE Trans. Ind. Electron.*, vol. 62, no. 7, pp. 4481–4491, Jul. 2015.
- [21] F. Yang, X. B. Ruan, Y. Yang, and Z. H. Ye, "Interleaved critical current mode boost PFC converter with coupled inductor," *IEEE Trans. Power Electron.*, vol. 26, no. 9, pp. 2404–2413, Sep. 2011.

- [22] P. L. Wong, P. Xu, B. Yang, and F. C. Lee, "Performance improvements of interleaving VRMs with coupling inductors," *IEEE Trans. Power Electron.*, vol. 16, no. 4, pp. 499–507, Jul. 2001.
- [23] Y. Dong, J. Zhou, F. C. Lee, M. Xu, and S. Wang, "Twisted core coupled inductors for microprocessor voltage regulators," *IEEE Trans. Power Electron.*, vol. 23, no. 5, pp. 2536–2545, May 2008.
- [24] Q. Li, Y. Dong, F. C. Lee, and D. J. Gilham, "High-density low-profile coupled inductor design for integrated point-of-load converters," *IEEE Trans. Power Electron.*, vol. 28, no. 1, pp. 547–554, Jan. 2013.
- [25] Y. Yang, D. Yan, and F. C. Lee, "A new coupled inductors design in 2-phase interleaving VRM," in *Proc. 6th IEEE Int. Power Electron. Motion Control Conf.*, May 2009, pp. 344–350.
- [26] G. Y. Zhu, B. McDonald, and K. R. Wang, "Modeling and analysis of coupled inductors in power converters," *IEEE Trans. Power Electron.*, vol. 26, no. 5, pp. 1355–1363, May 2011.
- [27] C. Wang, "Investigation on interleaved boost converters and applications," Ph.D. dissertation, Virginia Polytechnic Inst. State Univ., Blacksburg, VA, USA, Jul. 2009.
- [28] M. Phattanasak, W. Kaewmanee, and P. Thounthong, "Study of two-phase interleaved boost converter using coupled inductors for a fuel cell," in *Proc. Int. Conf. Electr. Eng./Electron., Comput., Telecommun. Inf. Technol.*, May 2013, pp. 1–6.
- [29] S. Ahsanuzzaman, T. McRae, M. Peretz, and A. Prodi, "Low-volume buck converter with adaptive inductor core biasing," in *Proc. IEEE Appl. Power Electron. Conf.*, Mar. 2012, pp. 335–339.
- [30] R. W. Erickson and D. Maksimovic, *Fundamentals of Power Electronics*. New York, NY, USA: Springer, 2000.
- [31] B. D. Cullity and C. D. Graham, *Introduction to Magnetic Materials*, 2nd ed. Hoboken, NJ, USA: Wiley, 2009.
- [32] EPCOS AG, "E16/8/5 (EF 16)," 2015. [Online]. Available: http://en.tdk.eu/inf/80/db/fer_13/e_16_8_5.pdf
- [33] EPCOS AG, "SIFERRIT material N87," Sep. 2006. [Online]. Available: <http://en.tdk.eu/blob/528882/download/4/pdf-n87.pdf>
- [34] Tridelta Magnet Systems GmbH, "Sintered NdFeB Magnets," 2016. [Online]. Available: http://www.tridelta.de/viomatrix/imgs/download/sintered_ndfeb_magnets.pdf
- [35] Coilcraft, "SER2000 Series High Current Shielded Power Inductors," 2016. [Online]. Available: <http://www.coilcraft.com/ser2000.cfm>



Zhigang Dang (S'14) received the B.Sc. degree in automation from Central South University, Hunan, China, in 2011, and the Master's degree in electrical engineering in December 2013 from The University of Alabama, Tuscaloosa, AL, USA, where he is currently working toward the Ph.D. degree in the Department of Electrical and Computer Engineering.

His research interests include wireless power transfer, power magnetics, and power electronics.



Jaber A. Abu Qahouq (SM'07) received the B.Sc. degree (with first class honors) from the Princess Sumaya University for Technology/Royal Scientific Society (RSS), Amman, Jordan, in 1998, and the M.S. and Ph.D. degrees from the University of Central Florida (UCF), Orlando, FL, USA, in 2000 and 2003, respectively, all in electrical engineering/electronics.

He is currently an Associate Professor in the Department of Electrical and Computer Engineering, College of Engineering, The University of Alabama, Tuscaloosa, AL, USA. Prior to his current position, he was with Intel Corporation, Hillsboro, OR, USA, UCF, and RSS. He is the author or coauthor of more than 100 refereed publications, two book chapters, and is a holder of 20 U.S. patents as of June 2016.

Dr. Abu Qahouq served as an IEEE Conference Technical Program Committee member for several conferences such as the IEEE Applied Power Electronics Conference and Exposition in 2013–2017. He received the King of Jordan Royal Watch in 1998, the IEEE Outstanding Graduate Student Award in 2002, the Division Recognition Award from Intel Corporation in 2006, and the Institution of Engineering and Technology Premium Award in 2009, among others.